Available online at www.sciencedirect.com
SCIENCE DIRECT®
Journal of Nuclear Materials 327 (2004) 27–36
journal of nuclear materials
www.elsevier.com/locate/jnucmat

Constituent redistribution in U–Pu–Zr fuel during irradiation

Yeon Soo Kim [a,*], G.L. Hofman [a], S.L. Hayes [b], Y.H. Sohn [c]

[a] *Argonne National Laboratory, 9700 S. Cass Ave, Argonne, IL 60439, USA*
[b] *Argonne National Laboratory, Idaho Falls, ID 83403-2528, USA*
[c] *University of Central Florida, 4000 Central Florida Blvd., Orlando, FL 32816-2455, USA*

Received 1 August 2003; accepted 9 January 2004

Abstract

The thermo-migration fluxes of U, Pu and Zr in U–Pu–Zr metallic alloy fuel during irradiation in the Experimental Breeder Reactor II (EBR-II) were calculated using the constituent redistribution profiles measured in postirradiation examinations. Based on these fluxes, the diffusion coefficients, and the sums of heat of transport and enthalpy of solution for the γ, $\gamma+\zeta$ and $\delta+\zeta$ phases in U–Pu–Zr were obtained. Using these data, the predicted concentration redistribution profiles are consistent with the measurements. The effect of minor actinide (Am and Np) addition was also examined. Am migration generally followed that of Zr with local precipitation, while Np behaved similarly to Pu.

1. Introduction

Constituent redistribution in a metallic alloy fuel can occur by solid-state diffusion under gradients of temperature and concentrations. This redistribution is also influenced significantly by irradiation and phase transformation. As a result, an originally uniformly mixed alloy can change to an inhomogeneous alloy. Inhomogeneity in a metallic nuclear fuel alloy can cause phase transformations, solidus temperature change, and local changes in fissile atom density, which can alter the physical and mechanical properties of the alloy fuel affecting its behavior and performance.

For metallic nuclear fuels, this phenomenon was observed as early as the 1960s. Murphy et al. [1] reported that irradiated U–Pu–Zr fuel rods showed three concentric microstructural zones containing different U and Zr concentrations in each zone. They suggested that the change in composition might be due to Zr migration only. Later Harbur et al. [2] found that out-of-pile annealing could result in constituent redistribution, indicating a thermal gradient alone could generate a driving force sufficient for constituent redistribution (i.e., Soret-type migration). During the course of the Integral Fast Reactor (IFR) fuel development effort, additional irradiation tests were carried out for U-based alloy fuels to reveal this phenomenon in detail [3–5]. The observations from these tests confirmed some features known before and also revealed new facts. The microstructures of the irradiated fuels commonly showed three distinct concentric zones: a Zr-enriched central zone, a Zr-depleted and U enriched intermediate zone, and a slightly Zr-enriched zone on the outer periphery. The annular zone structure was due not only to differences in porosity, but also to local composition changes. Although Pu appeared to be relatively immobile, its presence in the alloy at levels greater than 8 wt% enhanced U and Zr migration. As suggested by Porter et al. [5], this may be related to the increase in the gas bubble swelling rate in the high-Pu content fuels. The elevated temperature in high porosity fuel also generates a favorable condition for constituent migration. This hypothesis is supported by the observation that the

* Corresponding author. Tel.: +1-630 252 3173; fax: +1-630 252 5161.
E-mail address: yskim@anl.gov (Y.S. Kim).

0022-3115/$ - see front matter © 2004 Elsevier B.V. All rights reserved.
doi:10.1016/j.jnucmat.2004.01.012

constituent redistribution tends to saturate at a burnup of only a few atomic percent, when rapid initial gas-driven swelling results in an inter-connected network of open porosity that releases most of the fission gases subsequently generated and greatly slows continued fuel swelling.

There have been several attempts to analyze the phenomenon of constituent redistribution for both U–Zr and U–Pu–Zr metallic alloy fuels. Ogawa and Iwai [6] analyzed the U–Zr system using Marino's method [7] where the one-dimensional Fick's equation was solved numerically. A qualitative suggestion regarding the effect of the addition of Pu in U–Zr was made. No experimental data were utilized to verify the model predictions. Hofman et al. [8] analyzed their postirradiation data to develop a model that predicts the redistribution in U–Zr fuel using a numerical method. Predicted results were parametrically compared to measured U and Zr redistribution profiles to obtain estimates for the necessary kinetic and/or thermo-kinetic coefficients.

Ishida et al. [9] extended the Marino model for the U–Zr binary system to the U–Pu–Zr ternary system. Assuming Pu was equally partitioned in U and Zr, they assessed a quasi-binary system numerically. Their model, however, predicted redistribution profiles that were shifted toward the fuel surface, which differed from measured profiles and was perhaps due to fuel temperature predictions that were too high. Sohn et al. [10] measured out-of-pile constituent redistribution of U–Pu–Zr alloys under temperature gradients alone and developed an analytical model. Their analysis was performed only for the high temperature γ (bcc) phase. With the exception of Sohn et al. [10], all of the works used numerical methods, where diffusion coefficients and heats of transport were largely treated as numerical parameters whose values were adjusted to reproduce the experimental results. Consequently, the kinetic and/or thermo-kinetic properties are still not available for the concentration and temperature ranges of interest for fuel applications.

The objective of the present work is to assess the kinetic and/or thermo-kinetic properties for irradiated U–Pu–Zr fuel based on redistribution profiles measured at the end of fuel life. By utilizing the method proposed by Sohn et al. [10], the constituent interdiffusion fluxes of U, Pu and Zr at the end of fuel life were calculated without the need or knowledge of ternary interdiffusion coefficients ($\widetilde{D}_{ij}^{k}$'s) and heats of transport ($\widetilde{Q}_i$). The calculated interdiffusion fluxes were, then, employed to obtain effective interdiffusion coefficients ($\widetilde{D}_i^{\text{eff}}$), $\widetilde{D}_{ij}^{k}$'s and $\widetilde{Q}_i$'s. The concentration profiles were numerically simulated using the calculated $\widetilde{D}_i^{\text{eff}}$'s and $\widetilde{Q}_i$'s for comparison with experimental profiles; excellent agreement was obtained. However, it should be noted that the effect of irradiation on constituent migration was implicitly included in values of calculated $\widetilde{D}_{ij}^{k}$, $\widetilde{D}_i^{\text{eff}}$'s and $\widetilde{Q}_i$'s. The effects of irradiation and porosity buildup due to swelling are the fundamental differences of the present study from the laboratory experiments [10]. Irradiation is known to enhance diffusion while the increase in porosity due to swelling inhibits diffusion. In such cases, the present investigation demonstrates that an increase in porosity prevails over the effect of irradiation. The results are also utilized to evaluate thermo-transport in a U–Pu–Zr system which includes small amounts of minor actinides (U–Pu–Zr–MA).

2. Irradiation experiments

The fuel pin selected for the present study was from an experimental subassembly irradiated during the IFR fuel development program [3–5]. The fuel pin was designated as T179 from experiment X419 and was composed of a single-piece fuel slug produced by the injection-casting method [11]. The fuel had the fabrication and operational parameters given in Table 1. The actual composition of the fuel in atom percent was 61 at.% U + 16 at.% Pu + 23 at.% Zr, with a nominal concentration of U–19Pu–10Zr (wt%).

The fuel element was irradiated in the Experimental Breeder Reactor II (EBR-II) for two consecutive cycles of 49 days (Run 133) and 43 days (Run 134) during which the fuel element reached an end-of-life burnup of 1.9 at.%.

3. Postirradiation examinations

Fig. 1 shows the cross sectional optical photomicrograph of the postirradiation fuel and the corresponding X-ray (K_α) intensity from U, Pu and Zr, obtained from electron probe microanalysis (EPMA) superimposed at

Table 1
Fuel fabrication and operation data for the fuel element T179

Fuel alloy nominal composition (wt%)	U–19Pu–10Zr
^{235}U concentration in U (%)	56.99
Fuel slug length (mm)	342.9
Fuel slug radius (mm)	2.16
Fuel slug density (g/cm^3)	15.8
Fuel smeared density (%)	72.3
Fuel-cladding gap material	Liquid Na
Sodium level above fuel (mm)	6.35
Cladding thickness (mm)	0.381
Fuel-cladding gap width (mm)	0.762
Linear heat rate (W/cm)	420
Subassembly coolant temperatures (°C)	Inlet: 371, outlet: 486
Subassembly coolant flow rate (l/s)	7

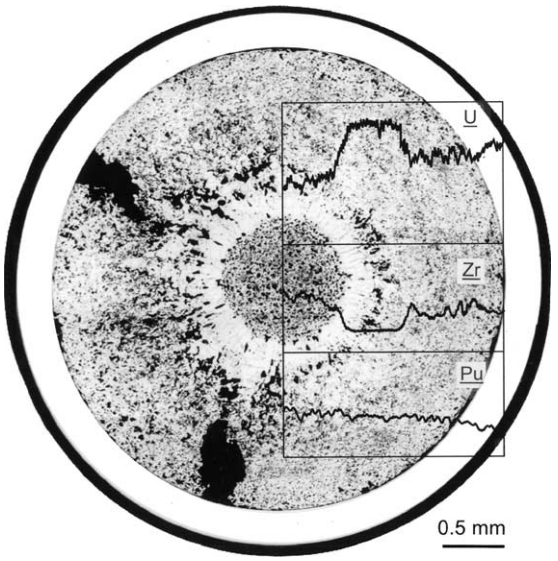

Fig. 1. Postirradiation optical metallography and measured constituent redistributions of T179 fuel at 1.9 at.% burnup.

an elevation of 230 mm ($z/L = 0.67$) from the bottom of the fuel. This axial location was chosen because it had the largest temperature gradient between the center and the surface. Indeed, Fig. 1 clearly shows three distinct concentric zones. At the center is the Zr-enriched zone with fission gas bubbles. The Zr concentration at the fuel center was 42 at.%, significantly higher than the initial concentration of 23 at.%. U was depleted from this zone significantly as the U concentration at the center was determined to be 38 at.%; a large decrease from the initial concentration of 61 at.%. Evidently, the intermediate zone was the densest, however detailed scanning electron microscopy has shown that this region also contains fine bubbles [12]. Large pores were also clustered in the intermediate zone, potentially due to fuel relocation. This zone had been depleted of Zr to 5 at.% and exhibited negligible concentration gradient. The outermost zone occupied the remaining portion of the fuel, where a slight Zr accumulation occurred and pores were mainly due to the tearing action between fuel grain boundaries.

Optical and scanning electron micrographs in Fig. 2 from the axial section of fuel show the pore morphology of the three zones. While large pores were observed in the center zone as shown in Fig. 2(c), the intermediate zone contained fine bubbles as shown in Fig. 2(b), and the outer zone shown in Fig. 2(d) exhibited the early stage of grain boundary tearing, which is due to anisotropic growth in the uranium grains. Because of the tearing action, pores in this zone are of irregular shape; not spherical normally seen for fission gas bubbles [12].

Pu concentration remained almost constant for all three zones with a slight decrease toward the fuel surface. From the ex-reactor annealing experiments of U–Pu–Zr alloys, Sohn et al. [10] showed that the small redistribution in the Pu concentration tended to follow that of U, while Meyer et al. [13] showed an almost

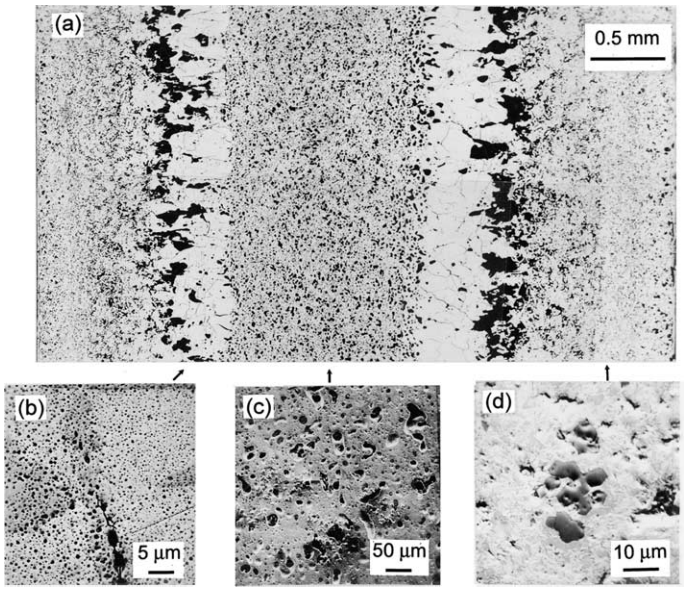

Fig. 2. Pore morphology of irradiated U–Pu–Zr fuel shown by optical metallography and SEM images: (a) optical micrograph of axial cross section, SEM images of (b) intermediate zone, (c) central zone, (d) outer zone.

negligible redistribution, although an extremely small decrease in the concentration of Pu was seen in their data close to the fuel surface.

The changes in the concentration of U and Zr, determined by EPMA, correspond well with the visually examined concentric zones and their boundaries. The first zone boundary near the fuel center is consistent with the inflection point on the concentration profiles for both U and Zr as seen in Fig. 1. The second zone boundary is not so clearly visible primarily because of the large pores in the middle of the zone. However, the inflection on the concentration profiles is clearer than the first one, especially for Zr as seen in Fig. 1. Combining the cross sectional view of the fuel and the concentration profiles, the two zone boundaries can be estimated at radial positions of 0.69 mm ($r/R = 0.32$) and 1.25 mm ($r/R = 0.58$) from the fuel center.

The U–19Pu–10Zr (wt%) alloy is known to form a bcc solid solution (γ-phase) in the temperature range of 650–750 °C [10,14]. In the temperature range of 600–650 °C, it exists as a mixture of γ- and ζ-phases. Below 600 °C, the γ-phase transforms to δ-phase, and the alloy is composed of δ- and ζ-phases in the temperature range of 500–600 °C [10]. According to Porter et al. [5], pure γ-phase occupied the central zone, a $\gamma + \zeta$ mixture existed in the intermediate zone, and a $\delta + \zeta$ mixture existed in the outer zone on postirradiation examinations. Therefore, in this investigation, the temperatures at the zone boundaries can be deduced as 650 °C for the $\gamma/(\gamma + \zeta)$ boundary and 600 °C for the $(\gamma + \zeta)/(\delta + \zeta)$ boundary. The effect of fission products and irradiation on phase stability was not considered in this paper because at the burnup level of the present case it would be negligible.

The fuel temperature varies due to changes in fuel thermal conductivity and power oscillations. In the initial state of irradiation, the fuel alloy has virtually no porosity and the power density is the highest. As burnup increases, the thermal conductivity of the fuel decreases due to porosity buildup as well as irradiation induced defects and fission product impurities, which causes the fuel temperature to rise. The linear power, however, continuously decreases at a rate of approximately 1% per 1 at.% burnup. Although these two factors offset each other to some extent, the temperature rises because the effect of the decrease in thermal conductivity dominates. As burnup increases further, the fuel swells and porosity develops and interconnects, which allow not only the escape of fission gas but also the logging of liquid bond sodium from the fuel-cladding gap into the fuel. Hofman et al. [15] reported that the pores become largely interconnected when the total porosity exceeds 33%. Based on the sodium balance data [15], on the average, the pores in the fuel were estimated about 7% filled with sodium at the end-of-life. Most of the logged sodium, however, is considered to reside in the pores near the fuel surface for the present case with a low burnup. Because sodium is a much better thermal conductor than the fuel alloy, a small amount of infiltrating sodium can increase the thermal conductivity significantly. The thermal conductivity in the fuel outer zone recovers the value of the unirradiated fuel.

The reactor power oscillations during the test were minimal not to impose changes in fuel temperature.

As a result, these factors make the fuel temperature stay within a narrow range for its duration in the reactor. Hofman and Walters [14] showed that the temperature at the fuel center near the end of fuel life for a typical EBR-II test is similar to the beginning-of-life value. The postirradiation fuel microstructure with three concentric zones highlighted by distinct phase boundaries is another evidence for the stable temperature distribution during irradiation. Similarly, the phase boundaries for the present case are considered unchanged during the power shutdown and startup between the two runs because time needed for the power reduction and the recover is much shorter than that needed for phase transformation.

Thus, zone boundary temperatures can be used to infer a more accurate radial temperature distribution from the viewpoint of constituent migration during irradiation [16]. Fig. 3 shows the temperature distribution in the fuel calculated based on the location of zone boundaries at the axial location of 230 mm from the fuel bottom ($z/L = 0.67$). The initial radial temperature distribution was also calculated and is shown for comparison in Fig. 3. The centerline temperature was estimated to change less than ~20 °C during the life of the fuel element. As seen in the figure, the largest change in temperature is estimated to have occurred near the mid-radius of the fuel.

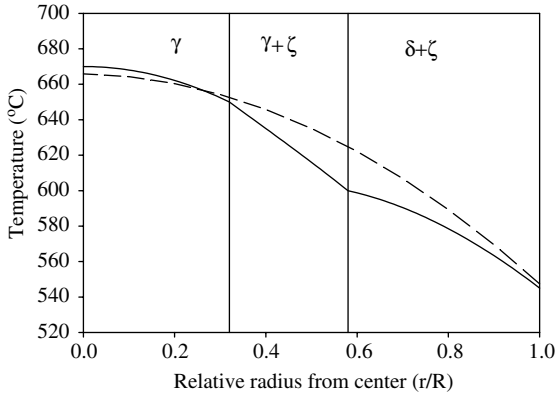

Fig. 3. Calculated temperature distributions of the fuel element T179 at the axial location $x/L = 0.67$ from the fuel bottom. The dashed line represents the beginning-of-life temperature and the solid line represents the temperature used in the analysis.

4. Analysis

4.1. Determination of interdiffusion fluxes

The fuel constituent redistribution profiles given in Fig. 1 were interpolated as smooth curves to minimize the local fluctuations of the microprobe signals caused by pores, precipitates and other defects. The radial mass conservation requirement for each constituent was applied and the total fractional concentration of the three constituents at a given location was normalized to unity. Axial constituent migration was assumed not to occur. The resulting concentration profiles are presented in Fig. 4. For analytical interpretation of the experimental data, the fuel was assumed to be a continuum.

The one-dimensional continuity equation for constituent i in cylindrical coordinates may be expressed as [17]

$$\frac{\partial C_i}{\partial t} = -\frac{1}{r}\frac{\partial(r\widetilde{J}_i)}{\partial r}, \tag{1}$$

where C_i is the concentration and $\widetilde{J}_i$ is the interdiffusion flux. The unit of the concentration in this study is in atom fraction and the corresponding unit for the flux is in atom fraction-meter per unit time. By using the parameter, $\lambda = r/\sqrt{t}$, where r is radius and t time, Eq. (1) can be integrated to give a relationship between the interdiffusion flux and concentration for component i

$$\widetilde{J}_i = \frac{1}{2t}\frac{1}{r}\int_{C_i^0}^{C_i(r)} r^2\,\mathrm{d}C_i, \tag{2}$$

where C_i^0 is the concentration of component i at the radial location of the laboratory-fixed frame. Detailed derivation of Eq. (2) from Eq. (1) is presented in Appendix A. Eq. (2) allows the determination of interdiffusion fluxes as a function of distance from the fuel center at a given time, without the knowledge of diffusion coefficients and heats of transport.

Using the concentration profiles presented in Fig. 4, Eq. (2) was employed to determine the interdiffusion fluxes at discretized radial locations. The results are presented in Fig. 5. In this figure, a negative diffusional flux corresponds to mass flow towards the center of the fuel. As seen in Fig. 5, Zr migrates toward the fuel center in the γ and most of $\gamma+\zeta$ phases and toward the fuel surface in the outer region of $\gamma+\zeta$ and $\delta+\zeta$ phases. U behaves in a manner almost opposite to Zr. The Pu flux is in general negative, but with small magnitude: slow migration towards the center of the fuel. The interdiffusion flux of Zr exhibits a zero flux plane (ZFP) where the net flux becomes zero, which occurs in the $\gamma+\zeta$ phase ($r/R = 0.545$) as identified in Fig. 5. U had two ZFPs: one at a similar location as Zr ($r/R = 0.545$) and the other close to the fuel surface ($r/R \sim 0.94$).

4.2. Determination of diffusion coefficients and heats of transport

For a ternary system (i–j–k) in radial gradients of temperature and concentration, as in Ref. [10], the interdiffusion flux of the component i in cylindrical coordinate can be expressed by

$$\widetilde{J}_i = -\beta_i\widetilde{Q}_i^{\gamma}\frac{C_i}{T}\frac{\partial T}{\partial r} - \widetilde{D}_{ii}^{k}\frac{\partial C_i}{\partial r} - \widetilde{D}_{ij}^{k}\frac{\partial C_j}{\partial r} \tag{3}$$

in a single phase, such as the γ-phase region, where β_i are the atomic mobilities, $\widetilde{Q}_i$ are the heats of transport, $\widetilde{D}_{ii}^{k}$ are the main (i.e., diagonal) interdiffusion coefficients, and $\widetilde{D}_{ij}^{k}$ are the cross (i.e., off-diagonal) interdiffusion coefficients with the third component k (i.e., for the present study, Pu) assumed to be the solvent. In the two-phase region, such as the $\gamma+\zeta$ phase, the partial

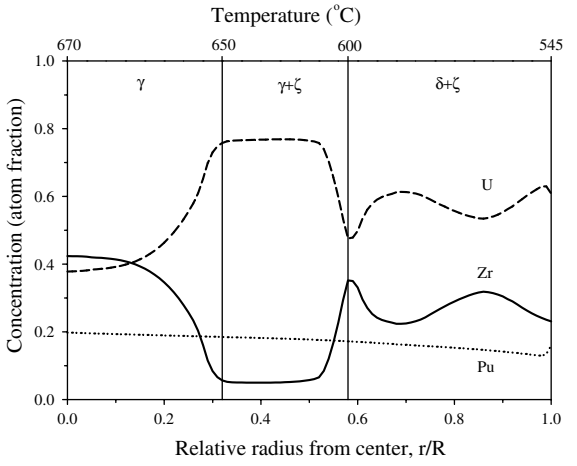

Fig. 4. Measured concentration profiles at 1.9 at.% burnup.

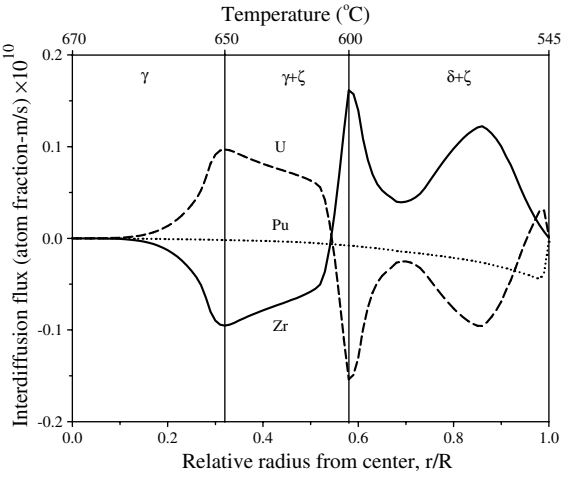

Fig. 5. Interdiffusion flux profiles at 1.9 at.% burnup.

enthalpy of solution of the component i in the alloy (ΔH_i) may be included in the expression for the interdiffusion flux as

$$\widetilde{J}_i = -\beta_i(\widetilde{Q}_i^{\gamma+\zeta} + \Delta H_i^{\gamma+\zeta})\frac{C_i}{T}\frac{\partial T}{\partial r} - \widetilde{D}_{ii}^{k}\frac{\partial C_i}{\partial r} - \widetilde{D}_{ij}^{k}\frac{\partial C_j}{\partial r}. \quad (4)$$

Similarly for the $\delta+\zeta$ two-phase region, the interdiffusion flux can be expressed as

$$\widetilde{J}_i = -\beta_i(\widetilde{Q}_i^{\delta+\zeta} + \Delta H_i^{\delta+\zeta})\frac{C_i}{T}\frac{\partial T}{\partial r} - \widetilde{D}_{ii}^{k}\frac{\partial C_i}{\partial r} - \widetilde{D}_{ij}^{k}\frac{\partial C_j}{\partial r}. \quad (5)$$

For a selected range of concentration, the second and third terms on the right hand side of Eqs. (3)–(5) can be expressed as a single term by defining the effective diffusion coefficient:

$$\widetilde{D}_i^{\text{eff}} = \widetilde{D}_{ii}^{k} + \widetilde{D}_{ij}^{k}\frac{\partial C_j}{\partial C_i}. \quad (6)$$

Then, Eqs. (3)–(5) can be written by

$$\widetilde{J}_i = -\beta_i\widetilde{Q}_i^{\gamma}\frac{C_i}{T}\frac{\mathrm{d}T}{\mathrm{d}r} - \widetilde{D}_i^{\text{eff}}\frac{\mathrm{d}C_i}{\mathrm{d}r}, \quad (7)$$

$$\widetilde{J}_i = -\beta_i(\widetilde{Q}_i^{\gamma+\zeta} + \Delta H_i^{\gamma+\zeta})\frac{C_i}{T}\frac{\partial T}{\partial r} - \widetilde{D}_i^{\text{eff}}\frac{\mathrm{d}C_i}{\mathrm{d}r} \quad (8)$$

and

$$\widetilde{J}_i = -\beta_i(\widetilde{Q}_i^{\delta+\zeta} + \Delta H_i^{\delta+\zeta})\frac{C_i}{T}\frac{\partial T}{\partial r} - \widetilde{D}_i^{\text{eff}}\frac{\mathrm{d}C_i}{\mathrm{d}r}. \quad (9)$$

From the experimental profiles of temperature, T, concentrations, C_i, and the corresponding fluxes, $\widetilde{J}_i$, Eqs. (7)–(9) were solved numerically for $\beta_i\widetilde{Q}_i^{\gamma}$ or $\beta_i(\widetilde{Q}_i^{\gamma+\zeta} + \Delta H_i^{\gamma+\zeta})$ or $\beta_i(\widetilde{Q}_i^{\delta+\zeta} + \Delta H_i^{\delta+\zeta})$ and $\widetilde{D}_i^{\text{eff}}$ at the 100 evenly divided radial locations.

The numerical solution for the determination of diffusion coefficients and heats of transport including the partial enthalpies of solution of the component for the two-phase regions proceeded according to the following scheme. Since there are four locations where the Zr redistribution profile exhibits local maximum or minimum in concentration ($\partial C_i/\partial r = 0$ at $r/R = 0.39$, 0.58, 0.68, and 0.86), the terms $\beta_i\widetilde{Q}_i^{\gamma}$ or $\beta_i(\widetilde{Q}_i^{\gamma+\zeta} + \Delta H_i^{\gamma+\zeta})$ or $\beta_i(\widetilde{Q}_i^{\delta+\zeta} + \Delta H_i^{\delta+\zeta})$ can be determined by rearranging Eqs. (7)–(9) as

$$\beta_i\widetilde{Q}_i^{\gamma} = -\frac{\widetilde{J}_i}{\dfrac{C_i}{T}\dfrac{\partial T}{\partial r}}, \quad (10a)$$

$$\beta_i(\widetilde{Q}_i^{\gamma+\zeta} + \Delta H_i^{\gamma+\zeta}) = -\frac{\widetilde{J}_i}{\dfrac{C_i}{T}\dfrac{\partial T}{\partial r}}, \quad (10b)$$

$$\beta_i(\widetilde{Q}_i^{\delta+\zeta} + \Delta H_i^{\delta+\zeta}) = -\frac{\widetilde{J}_i}{\dfrac{C_i}{T}\dfrac{\partial T}{\partial r}}. \quad (10c)$$

Similarly for U, there are also four such locations ($r/R = 0.44$, 0.58, 0.70, 0.87, and 0.98) where the terms $\beta_i\widetilde{Q}_i^{\gamma}$ or $\beta_i(\widetilde{Q}_i^{\gamma+\zeta} + \Delta H_i^{\gamma+\zeta})$ or $\beta_i(\widetilde{Q}_i^{\delta+\zeta} + \Delta H_i^{\delta+\zeta})$ can be determined. However, $\widetilde{D}_i^{\text{eff}}$ is not determined by Eqs. (10a)–(10c) at these locations: a value must be guessed. For the locations between these local maximums or minimums in concentration, $\beta_i\widetilde{Q}_i^{\gamma}$ or $\beta_i(\widetilde{Q}_i^{\gamma+\zeta} + \Delta H_i^{\gamma+\zeta})$ or $\beta_i(\widetilde{Q}_i^{\delta+\zeta} + \Delta H_i^{\delta+\zeta})$ together with $\widetilde{D}_i^{\text{eff}}$ are estimated numerically using Eqs. (7)–(9). It was assumed that $\widetilde{D}_i^{\text{eff}}$ increases as T increases.

The zero flux location was identified at $r/R = 0.545$ for Zr, and at $r/R = 0.545$ and 0.955 for U, where the interdiffusion fluxes become zero. At these locations, Eqs. (8) and (9) can be expressed as

$$\frac{\beta_i(\widetilde{Q}_i^{\gamma+\zeta} + \Delta H_i^{\gamma+\zeta})}{\widetilde{D}_i^{\text{eff}}} = \frac{\dfrac{\partial C_i}{\partial r}}{\dfrac{C_i}{T}\dfrac{\partial T}{\partial r}}, \quad (11)$$

$$\frac{\beta_i(\widetilde{Q}_i^{\delta+\zeta} + \Delta H_i^{\delta+\zeta})}{\widetilde{D}_i^{\text{eff}}} = \frac{\dfrac{\partial C_i}{\partial r}}{\dfrac{C_i}{T}\dfrac{\partial T}{\partial r}}. \quad (12)$$

The right hand side of Eq. (11) or Eq. (12) is obtained directly from the data and the left hand side is a result of the guessed values. The value of the guess and the above calculation process are repeated until the two values of each side of Eq. (11) converge.

In addition, the interdiffusion fluxes become negligible near the fuel center based on the choice of laboratory-fixed frame employed in this study, although the gradients in C and T are not negligible. Therefore, near the fuel center, Eq. (11) was employed to estimate the ratio $\beta_i\widetilde{Q}_i^{\gamma}/\widetilde{D}_i^{\text{eff}}$. For example, at $r/R = 0.02$, $\beta_{\text{Zr}}\widetilde{Q}_{\text{Zr}}^{\gamma}/\widetilde{D}_{\text{Zr}}^{\text{eff}} = -12.6$ and $\beta_{\text{U}}\widetilde{Q}_{\text{U}}^{\gamma}/\widetilde{D}_{\text{U}}^{\text{eff}} = 33.0$. This ratio was almost constant for r/R in the range of 0–0.1 and provided an input for the numerical estimation of diffusion coefficients and heats of transport in the γ-phase near the fuel center.

The calculated values for the effective diffusion coefficients and heats of transport as a function of the distance from the fuel center are plotted in Fig. 6 for Zr and U.

The average diffusion properties over the entire phase regions, γ, $\gamma+\zeta$, and $\delta+\zeta$ were also calculated for comparison with the values reported in the literature. The volume average values of $\beta_i\widetilde{Q}_i^{\gamma}$, $\overline{\beta_i(\widetilde{Q}_i^{\gamma+\zeta} + \Delta H_i^{\gamma+\zeta})}$, $\overline{\beta_i(\widetilde{Q}_i^{\delta+\zeta} + \Delta H_i^{\delta+\zeta})}$ and $\overline{\widetilde{D}_i^{\text{eff}}}$ for each phase region were calculated from the values plotted in Fig. 6 and are reported in Table 2. The values determined at the locations where the local maxima or minima in concentrations occur are also included in the table.

At $r/R = 0.39$, 0.58, 0.68, and 0.86 for Zr and $r/R = 0.44$, 0.58, 0.70, and 0.87 for U, $\partial C_i/\partial r = 0$. At

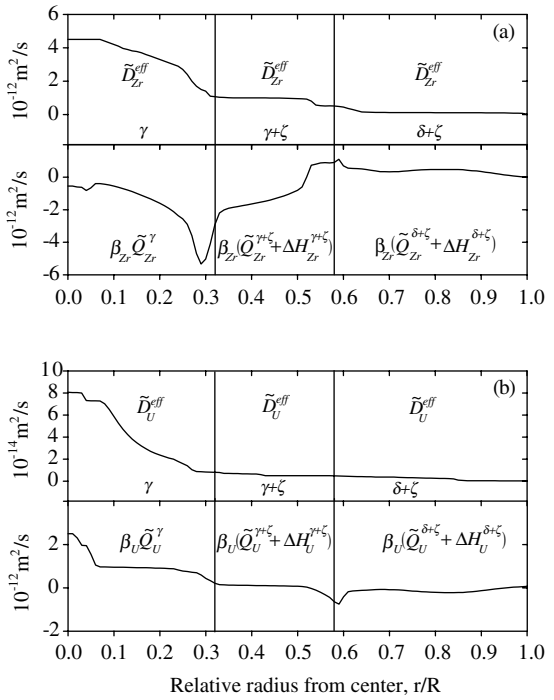

Fig. 6. Calculated interdiffusion properties: (a) Zr and (b) U.

these locations, interdiffusion coefficients can be estimated. For the locations in the $\gamma+\zeta$ phase, Eq. (4) becomes

$$\widetilde{J}_i = -\beta_i(\widetilde{Q}_i^{\gamma+\zeta} + \Delta H_i^{\gamma+\zeta})\frac{C_i}{T}\frac{\partial T}{\partial r} - \widetilde{D}_{ij}^{\mathrm{Pu}}\frac{\partial C_j}{\partial r}. \tag{13}$$

By solving for $\widetilde{D}_{ij}^{\mathrm{Pu}}$, we obtain

$$\widetilde{D}_{ij}^{\mathrm{Pu}} = \frac{\widetilde{J}_i + \beta_i(\widetilde{Q}_i^{\gamma+\zeta} + \Delta H_i^{\gamma+\zeta})\dfrac{C_i}{T}\dfrac{\partial T}{\partial r}}{-\dfrac{\partial C_j}{\partial r}}. \tag{14}$$

By rearranging Eq. (6), we also obtain

$$\widetilde{D}_{ii}^{\mathrm{Pu}} = \widetilde{D}_i^{\mathrm{eff}} - \widetilde{D}_{ij}^{\mathrm{Pu}}\frac{\partial C_j}{\partial C_i}. \tag{15}$$

For the locations in the $\delta+\zeta$ phase, the same method was used to extract the interdiffusion coefficients. The values obtained for $\widetilde{D}_{\mathrm{ZrZr}}^{\mathrm{Pu}}$, $\widetilde{D}_{\mathrm{ZrU}}^{\mathrm{Pu}}$, $\widetilde{D}_{\mathrm{UZr}}^{\mathrm{Pu}}$, and $\widetilde{D}_{\mathrm{UU}}^{\mathrm{Pu}}$ are provided in Table 3. The interdiffusion coefficients for the γ-phase could not be derived in the current method because there is no concentration maximum or minimum in the γ-phase. Although the obtained values are for several specific locations, they provide a good method to check the validity of the calculations. The calculated values are consistent with the approximate ranges suggested by Ishida et al. [9], and generally lower than the values reported by Sohn et al. [10] since the present values are for the lower temperature phases.

4.3. Predictions of constituent redistribution profiles

The concentration profiles developed during irradiation of the T179 fuel element to 1.9 at.% burnup were calculated using the effective interdiffusion coefficients and heats of transport presented in Fig. 6. In Fig. 7, the calculated concentration profiles are compared with the measured profiles. For all components, experimental and predicted profiles are generally in good agreement for all locations except near the fuel surface. The

Table 2
Average diffusion properties calculated based on the component redistribution of the T179 fuel element and the corresponding temperature distribution

Phase	$\frac{r}{R}$	$\overline{\beta_i\widetilde{Q}_i^{\gamma}}$ (10^{-13} m²/s atom)			$\overline{\widetilde{D}_i^{\mathrm{eff}}}$ (10^{-15} m²/s)		
		Zr	U	Pu	Zr	U	Pu
γ	$0 \leftrightarrow 0.32$	−24.3	9.2	−0.4	27.8	31.3	10.8
		$\overline{\beta_i(\widetilde{Q}_i^{\gamma+\zeta} + \Delta H_i^{\gamma+\zeta})}$ (10^{-13} m²/s atom)			$\overline{\widetilde{D}_i^{\mathrm{eff}}}$ (10^{-15} m²/s)		
$\gamma+\zeta$	$0.32 \leftrightarrow 0.58$	−7.8	−0.3	−0.4	8.7	7.4	10.1
$\partial C_i/\partial r = 0$	0.39	−18.5	na	na	na	na	na
$\partial C_i/\partial r = 0$	0.44	na	1.0	na	na	na	na
		$\overline{\beta_i(\widetilde{Q}_i^{\delta+\zeta} + \Delta H_i^{\delta+\zeta})}$ (10^{-13} m²/s atom)			$\overline{\widetilde{D}_i^{\mathrm{eff}}}$ (10^{-15} m²/s)		
$\delta+\zeta$	$0.58 \leftrightarrow 1$	3.7	−1.2	−2.5	1.4	2.8	7.0
$\partial C_i/\partial r = 0$	0.58	6.5	−6.4	na	na	na	na
$\partial C_i/\partial r = 0$	0.69	3.5	na	na	na	na	na
$\partial C_i/\partial r = 0$	0.70	na	−0.8	na	na	na	na
$\partial C_i/\partial r = 0$	0.86	4.6	na	na	na	na	na
$\partial C_i/\partial r = 0$	0.87	na	−1.9	na	na	na	na

Table 3
Main and cross interdiffusion coefficients calculated for the redistribution of the constituents and temperature

Radial location (r/R)	$\widetilde{D}^{Pu}_{ZrZr}$ (10^{-14} m^2/s)	$\widetilde{D}^{Pu}_{ZrU}$ (10^{-14} m^2/s)	$\widetilde{D}^{Pu}_{UZr}$ (10^{-14} m^2/s)	$\widetilde{D}^{Pu}_{UU}$ (10^{-14} m^2/s)
0.39	3.4	0.25	na	na
0.44	na	na	0.44	4.0
0.69	0.49	0.068	na	na
0.70	na	na	0.11	0.69
0.86	0.24	0.085	na	na
0.87	na	na	0.10	0.33

These values were calculated at the local concentration maximum and minimum locations.

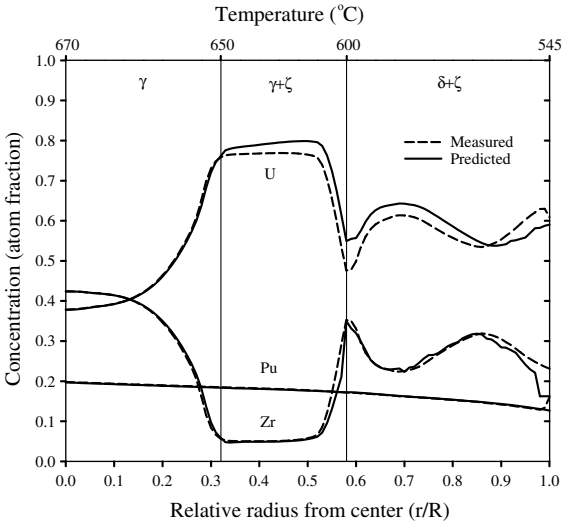

Fig. 7. Comparison of measured and calculated constituent concentration profiles.

discrepancy near the fuel surface may be attributed to the complexity of the fuel matrix due to swelling and to the existence of a Zr-rich layer at the fuel surface (i.e., a 20-μm-thick layer with ~60 at.% Zr due to fuel-cladding chemical interactions [14]). However, for simplicity, this Zr content was excluded from the measured concentration profiles and subsequent analysis because it represents a negligible driving force for constituent redistribution.

5. Minor actinide addition

U–Pu–Zr fuels with small (1.2–1.3 wt%) minor actinide (MA) additions, Am and Np, were also irradiated with EBR-II [13]. Fig. 8 shows a postirradiation optical micrograph and the corresponding constituent redistribution profiles. These tests revealed that small additions of MA did not alter the redistribution characteristics of U, Pu, and Zr from U–Pu–Zr fuels without MA. The EPMA signal corresponding to Am slightly increased at the fuel center and outer region, which suggests that the trend of Am redistribution is similar to that of Zr.

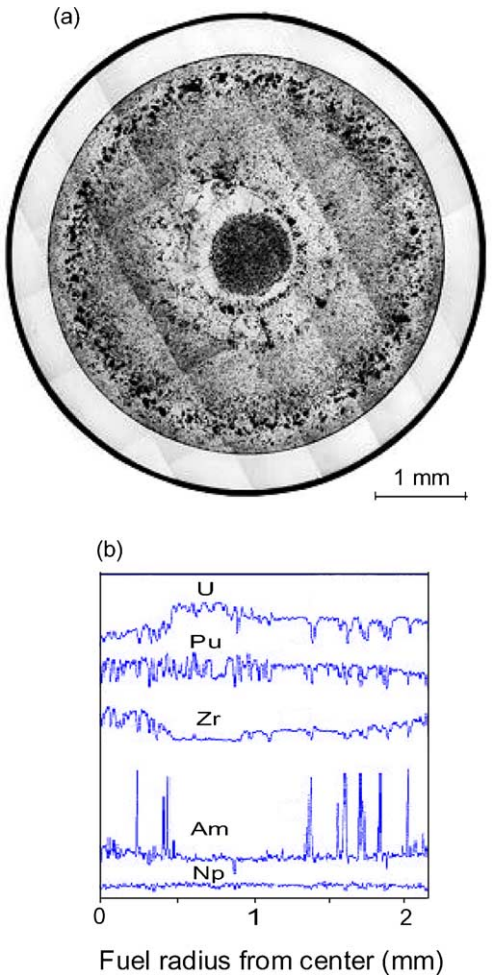

Fig. 8. Postirradiation results of X501 test [13]: (a) optical image of the fuel cross section, (b) concentration redistribution measured by EPMA. The fuel was composed of U–20.2Pu–9.1Zr–1.2Am–1.3Np (wt%) and irradiated to ~6 at.% burnup.

It is also remarkable that Am precipitated in regions where high porosity was observed. Strong EPMA signals correspond to locations where U, Pu, and Zr signals dropped. This implies that Am migrated to the fuel center and the fuel outer regions, where large intercon-

nected pores were available. Am segregation may have been facilitated by large pores in the irradiated fuel since Am could not be detected in the intermediate region where large pores were absent. This also explains why the Am segregation was observed at the fuel center region, which is the hottest part of the fuel [18].

Np, however, did not exhibit any significant redistribution or precipitation behavior like Am. This is consistent with the finding by Kurata et al. [19].

6. Conclusions

U–Pu–Zr metallic alloy fuel exhibits three distinct phase regions during operation. For a fuel composition of U–19Pu–10Zr, the center region was composed of γ (above 650 °C), the intermediate region of $\gamma + \zeta$ (600–650 °C), and the outer region of $\delta + \zeta$ (500–600 °C) phases. Thermally activated constituent migration took place in the initially homogeneous fuel, and then, as concentration gradient builds up, migration due to concentration gradients followed. The fuel temperature was estimated to remain almost unchanged during irradiation.

Based on the postirradiation measured redistribution profiles, the interdiffusion fluxes of Zr, U and Pu in U–Pu–Zr fuel at a particular time were calculated without using diffusion coefficients or heats of transport. These fluxes were used to assess interdiffusion coefficients and heats of transport as a function of radial positions with the fuel.

The data obtained from the analyses were evaluated by reconstructing the concentration profiles and comparing with the measured. The model calculations for concentration redistributions were very consistent with the measured ones, validating the accuracy of the present model.

The effect of small amounts of minor actinide additions to U–Pu–Zr is negligible from the viewpoint of constituent redistribution. Am was observed to migrate throughout the fuel cross section. The Am redistribution profile indicates that its tendency resembles that of Zr migration; the only difference is its segregation showing large peaking signals at the fuel center and surface regions. The Np behavior is similar to that of Pu. From this observation, it is recommended that Am be considered to follow Zr and Np to follow Pu where simple calculations are needed.

Acknowledgements

This work has been created by the University of Chicago as Operator of Argonne National Laboratory under contract no. W-31-109-ENG-38 with the US Department of Energy.

Appendix A

$$\frac{\partial C}{\partial t} = -\frac{1}{r}\frac{\partial(r\widetilde{J})}{\partial r}. \tag{A.1}$$

By using the parameter, $\lambda = r/\sqrt{t}$, we obtain

$$\mathrm{d}t = -\frac{2t\sqrt{t}}{r}\mathrm{d}\lambda, \tag{A.2}$$

$$\mathrm{d}r = \sqrt{t}\mathrm{d}\lambda. \tag{A.3}$$

Substitution of Eqs. (A.2) and (A.3) in Eq. (A.1) yield

$$\frac{\mathrm{d}C}{-\dfrac{2t\sqrt{t}}{r}\mathrm{d}\lambda} = -\frac{1}{r}\frac{\mathrm{d}(r\widetilde{J})}{\sqrt{t}\mathrm{d}\lambda},$$

which leads to

$$\frac{r^2}{2t}\frac{\mathrm{d}C}{\mathrm{d}\lambda} = \frac{\mathrm{d}(r\widetilde{J})}{\mathrm{d}\lambda}. \tag{A.4}$$

Integrating Eq. (A.4) gives

$$\int \mathrm{d}(r\widetilde{J}) = \frac{1}{2t}\int r^2\,\mathrm{d}C. \tag{A.5}$$

By noticing $\widetilde{J} = 0$ at $r = 0$, Eq. (A.5) can be rearranged as

$$\widetilde{J} = \frac{1}{2t}\frac{1}{r}\int_{C^0}^{C(r)} r^2\,\mathrm{d}C. \tag{A.6}$$

References

[1] W.F. Murphy, W.N. Beck, F.L. Brown, B. Koprowski, L.A. Neimark, Postirradiation examination of U–Pu–Zr fuel elements irradiated in EBR-II to 4.5 atomic percent burnup, Argonne National Laboratory, Report ANL-7602, 1969.
[2] D.R. Harbur, J.W. Anderson, W.J. Maraman, Studies on the U–Pu–Zr alloy system for fast breeder reactor application, Los Alamos Scientific Laboratory, Report LA-4512, 1970.
[3] R.G. Pahl, C.E. Lahm, R. Villareal, W.N. Beck, G.L. Hofman, in: Proceedings of the International Conference on Reliable Fuels for Liquid Metal Reactors, Tucson, AZ, USA, 7–11 September 1986.
[4] R.G. Pahl, D.L. Porter, C.E. Lahm, G.L. Hofman, Metall. Trans. A 21A (1990) 1863.
[5] D.L. Porter, C.E. Lahm, R.G. Pahl, Metall. Trans. A 21A (1990) 1871.
[6] T. Ogawa, T. Iwai, J. Less-Common Metals 175 (1991) 59.
[7] G.P. Marino, Nucl. Sci. Eng. 49 (1972) 93.
[8] G.L. Hofman, S.L. Hayes, M.C. Petri, J. Nucl. Mater. 227 (1996) 277.

[9] M. Ishida, T. Ogata, M. Kinoshita, Nucl. Technol. 104 (1993) 37.
[10] Y.H. Sohn, M.A. Dayananda, G.L. Hofman, R.V. Strain, S.L. Hayes, J. Nucl. Mater. 279 (2000) 317.
[11] B.R. Seidel, D.B. Tracy, V. Griffiths, Methods and apparatus for injection casting metallic nuclear energy fuel rods, Argonne National Laboratory, Report PATENTS-US-A7333935, 1989.
[12] G.L. Hofman, R.G. Pahl, C.E. Lahm, D.L. Porter, Metal. Trans. A 21A (1990) 517.
[13] M.K. Meyer, S.L. Hayes, D.C. Crawford, R.G. Pahl, H. Tsai, in: Proceedings of the ANS Conference on Accelerator Applications in the New Millennium, Reno, NV, 11–15 November 2001.
[14] G.L. Hofman, L.C. Walters, in: R.W. Cahn, P. Haasen, E.J. Kramer (Eds.), Materials Science and Technology, vol. 10A, VCH, New York, 1993, p. 23.
[15] G.L. Hofman, W.N. Beck, R.V. Strain, G.O. Hayner, C.M. Walter, Irradiation behavior of unencapsulated EBR-II MARK-II driver fuel to a maximum burnup of 6 at%, Argonne National Laboratory, Report ANL-8119, 1976.
[16] A.M. Yacout, G.L. Hofman, Y. Orechwa, S. Salvatores, Trans. Am. Nucl. Soc. 68 (1993) 98.
[17] R.B. Bird, W.E. Stewart, E.N. Lightfoot, Transport Phenomena, John Wiley, 1960, p. 83.
[18] Y.S. Kim, G.L. Hofman, Argonne National Laboratory, Report ANL-AAA-068, 2003.
[19] M. Kurata, T. Inoue, C. Sari, J. Nucl. Mater. 208 (1994) 144.